

# Dispersive modeling of breaking waves on a slope

Jihwan Kim<sup>a</sup>, Geir K. Pedersen<sup>a</sup>, Finn Løvholt<sup>a,b</sup>, Randall J. LeVeque<sup>c</sup>

<sup>a</sup>*University of Oslo, Department of Mathematics, Oslo, Norway*

<sup>b</sup>*Norwegian Geotechnical Institute, Oslo, Norway*

<sup>c</sup>*University of Washington, Department of Applied Mathematics, Seattle, USA*

---

## Abstract

The nonlinear shallow water model is widely used in the study of tsunami propagations, but an increasing number of studies are dedicated to the dispersion dynamics of tsunamis. If the wave dispersion becomes important, Boussinesq-type models are often used. In this work, an operational Boussinesq solver, *BoussClaw*, is introduced for modeling fully non-linear dispersive tsunami propagation, taking into account inundation. In the *BOUSSCLAW* model, Boussinesq equations from the literatures, based on the depth-averaged velocity and with enhanced dispersion properties, are implemented using a hybrid of the finite volume and finite difference methods. In order to validate *BOUSSCLAW*, numerical results are compared to the analytical solutions and laboratory experiments. Furthermore, the wave steepening and breaking motion is explored with the help of the full potential boundary integral model, and we demonstrate that the point of wave breaking may be misinterpreted in Boussinesq models.

*Keywords:* Breaking wave, Boussinesq equation, finite volume method

---

## 1. Introduction

Tsunamis are often considered as long waves compared to the water depth, and depth-averaged wave models are consequently widely used in the study of their propagation and inundation. Through the use of numerical shock capturing techniques for modeling the nearshore bore formation of the tsunami, *nonlinear*  
5 *shallow water* (NLSW) models have become the standard model for modeling

tsunami propagation and run-up, see e.g. (Titov and Synolakis, 1995; Imamura, 1996; Harig et al., 2008; Berger et al., 2011). Well known applications include inundation modeling of the recent major tsunami events such as the 2004 Indian Ocean tsunami (Borrero et al., 2006; Kaiser et al., 2011) and the 2011 Tohoku tsunami (Hooper et al., 2013; Romano et al., 2014).

The NLSW models do not incorporate frequency dispersion and are valid only for large wavelength-to-depth-ratios ( $\lambda/h > 20$ ). The accumulated effect of the frequency dispersion for the wave propagation over the open sea is a function of propagation time and the shape of the disturbance (Glimsdal et al., 2013), and may become important for some tsunamis, in particular for landslide sources (Løvholt et al., 2015). Dispersion may further be of importance, in combination with non-linear effects, for the evolution of undular bores (Behrens and Dias, 2015). *Boussinesq-type models* that allow for more accurate modeling of shorter waves, may be used to model dispersive tsunamis. In the last decades we have seen a development on long wave expansions and their numerical formulations. New Boussinesq type formulations, such as those introduced by Madsen and Sørensen (1992), and Nwogu (1993), displayed improved accuracy, as well as extended validity ranges in comparison to the standard formulation of Peregrine (1967).

In their original formulation, Boussinesq-type models do not take into account the post-breaking motion. In order to combine breaking with the Boussinesq-type equations several strategies have therefore been suggested. For instance, Peregrine (1967) used  $A/h = 0.6$  as the break threshold, while pointing out that this value could reach around 2 in laboratory experiments. Another way of incorporating the breaking that was suggested by Kennedy et al. (2000) included diffusive terms in the momentum equation to smear out sharp fronts. Løvholt et al. (2013) similarly employed a diffusive model including transport terms, but pointed out that breaking wave Boussinesq models were prone to instabilities. Schäffer et al. (1993) introduced the concept of the *surface roller*. Lynett (2006) investigated  $\eta_t/c$ ,  $\eta_x$ ,  $u_{xx}H^2/c$ , and  $u/c$ , where  $c = \sqrt{gH}$ ,  $u$  is the wave speed and  $\eta$  is the water surface elevation, and then identified that the critical

front slope ( $\eta_x$ ) is the least sensitive breaking threshold. Tissier et al. (2012) suggested a breaking decision model based on the surface roller, the maximal  
40 front angle and the Froude number. An alternative non-linear diffusive ad-hoc breaking term was suggested Matsuyama et al. (2007), based on their large scale experiments of the wave propagation of undular bores on various slope angles.

Recent developments of operational Boussinesq models, have made use of more sophisticated hybrid numerical techniques such as use of approximate  
45 Riemann solvers combined with TVD limiters for the conserved variables, and finite differences for additional higher order terms (Erduran et al., 2005; Kim et al., 2009; Shi et al., 2012), leading among others to the popular FUNWAVE-TVD and COULWAVE-TVD applications. For instance in Shi et al. (2012), Boussinesq terms are switched off the near-shore region where large amplitude-  
50 to-depth-ratios occur, implying that only NLSW terms remain in the shallowest region. This allows for a relatively robust treatment of the modeling of the post breaking phase. To this end, the  $A/h = 0.8$  threshold suggested by (Shi et al., 2012) based on the Froude similarity analysis by Tonelli and Petti (2009), have in many ways become the standard for incorporating breaking in a feasible and  
55 practical way.

In this paper, we present a new hybrid Boussinesq type model BOUSSCLAW, of similar mould as FUNWAVE-TVD and COULWAVE-TVD. The emphasis is twofold. First, to present a careful validation of the model, both towards laboratory experiments and more general reference models. Second, we use the  
60 new model in comparison with a full potential reference model to explore how accurate the Boussinesq models can represent the wave evolution until the point of breaking. In the present example, we are finally able to demonstrate that Boussinesq models may be employed to accurately model the near shore tsunami propagation beyond the standard  $A/h = 0.8$  threshold depth. Conversely, we  
65 find that the use of the standard  $A/h = 0.8$  threshold depth invokes a too early formation of a breaking bore. This points out that that the breaking criteria employed so far lacks generality.

This paper is organized as follows: In Section 2, the base model for the

wave equations is given and the numerical scheme is outlined, including a von  
70 Neuman stability analysis. Section 3 compares results from the BOUSSCLAW  
with the analytic solutions and laboratory experiments. Section 4 discusses the  
wave steepening and using a Boundary Integral Method (BIM) for solving the  
full potential equations. In Section 5, we compare these results of pre-breaking  
evolution with Boussinesq type models.

## 75 2. Model Description

Boussinesq-type equations include non-hydrostatic pressure in an approxi-  
mate way treat short waves more accurately than the shallow water equations.  
The Boussinesq-type wave models have been derived on the assumption that  
 $\mathcal{O}(\epsilon)$  and  $\mathcal{O}(\mu)$  terms are small, where  $\epsilon$  and  $\mu$  denote the ratio of wave am-  
80 plitude to depth and the ratio of depth to wavelength respectively. Various  
models have been suggested, and the papers of Peregrine (1967), Madsen and  
Sørensen (1992), Nwogu (1993), Lynett et al. (2002), and Wei and Kirby (1995)  
are representative examples.

In this work, a new numerical model, called BOUSSCLAW, is introduced. It is  
85 an extension of GEOCLAW Clawpack Development Team (2016), and solves the  
Boussinesq-type equations derived by Schäffer et al. (1993). The BOUSSCLAW  
model is a hybrid of the finite volume and finite difference solvers with the  
operation splitting technique. The GEOCLAW software is a part of Clawpack  
Development Team (2016) developed mainly by by LeVeque (1997), George  
90 (2008) and Berger et al. (2011) which is designed to solve the nonlinear shallow  
water equations.

### 2.1. BOUSSCLAW - a new long wave model for tsunami propagation and run-up

#### 2.1.1. Boussinesq-type equations

Schäffer et al. (1993) derived Boussinesq-type equations with an addition of

a Padé approximation of the linear dispersion relation. The equations read

$$H_t + (Hu)_x = 0, \quad (1)$$

$$(1 - D)[(Hu)_t] + \left(Hu^2 + \frac{g}{2}H^2\right)_x - gHh_x - Bgh^2(h\eta_x)_{xx} = 0, \quad (2)$$

where the operator  $D$  is defined as

$$D(w) = \left(B + \frac{1}{2}\right)h^2w_{xx} - \frac{1}{6}h^3\left(\frac{w}{h}\right)_{xx}, \quad (3)$$

for any  $w(x, t)$ . In the above equations  $H(x, t)$  and  $u(x, t)$  are the total flow  
95 depth and the depth averaged velocity of the water, respectively,  $h(x)$  is the still  
water depth,  $\eta(x, t)$  is the surface elevation, and thus  $H(x, t) = h(x) + \eta(x, t)$ .  
Moreover,  $g$  is the acceleration of gravity, and  $B$  is a dispersion parameter. Mad-  
sen and Sørensen (1992) has chosen the parameter  $B = 1/15$  from a Padé expan-  
sion of the linear dispersion analysis. When  $B = 0$ , this set of the Boussinesq-  
100 type equations approximately reduces to that of Peregrine (1967) as the linear  
dispersion relations are identical. However, unlike Peregrine's momentum equa-  
tion the hydrostatic parts of (2) are written in a conservative form. Moreover,  
some nonlinearity is introduced in the dispersion term for convenience. Even  
though (1), (2) and (3) do not constitute a fully nonlinear set of Boussinesq,  
105 they do describe shoaling of solitary waves markedly better than, for instance,  
Peregrine equations, as will be demonstrated in section 5.

The BOUSSCLAW model solves the Boussinesq-type equations (1) and (2)  
numerically with a hybrid combination of the finite volume and finite difference  
methods that will be explained in a moment. There have been several studies  
110 on this type of hybrid schemes. For example, see Tissier et al. (2011), Shi et al.  
(2012) and Dutykh et al. (2013).

To facilitate a fractional step method, as outlined below, we move the hy-  
drostatic terms of (2) inside the  $(1 - D)$  operator, while balancing with extra  
terms in the  $\Psi$ , to obtain

$$(1 - D)[(Hu)_t] + \left(Hu^2 + \frac{g}{2}H^2\right)_x - gHh_x = -\Psi(x, t), \quad (4)$$

where

$$\begin{aligned} \Psi(x, t) = & \left( B + \frac{1}{2} \right) h^2 \left( (Hu^2)_x + gH\eta_x \right)_{xx} \\ & - \frac{1}{6} h^3 \left( \frac{(Hu^2)_x + gH\eta_x}{h} \right)_{xx} - Bgh^2 (h\eta_x)_{xx}. \end{aligned} \quad (5)$$

### 2.1.2. Numerical scheme

The equations (1) and (4) are written in a form that conserves momentum to leading order in  $\mu$ , but with the  $\Psi$  term as a pseudo source. Such equations may be solved by a *fractional step method* as described in LeVeque (2002), for instance. First, it is observed that (4) may be formally rewritten as

$$(Hu)_t = - \left\{ \left( Hu^2 + \frac{g}{2} H^2 \right)_x - gHh_x \right\} - (1 - D)^{-1} \Psi(x, t), \quad (6)$$

At the first stage of the hybrid scheme, we integrate  $Hu$  over a time step taking into account all hydrostatic terms, namely those within the braces on the right  
115 hand side, and omitting the source terms involving  $\Psi$ . When this is combined with the continuity equation (1) this simply corresponds to advancing the shallow water equations one time step forward. To this end we employ GEOCLAW, a high-order accurate finite volume solver for the shallow water equations with adaptive mesh refinements.

In the second stage, we retain the new  $H$  value, but integrate  $Hu$  (essentially being the momentum density) further from the first stage by solving

$$(1 - D) [(Hu)_t] = -\Psi. \quad (7)$$

120 Since the differential operator  $D$  contains spatial derivatives, a systems of difference equations must then be solved.

The spatial and time discretization should be carefully chosen for the stability of the second stage. In our numerical scheme, the second order centered scheme is used for the spatial discretization, and a four stage Runge-Kutta  
125 method is used for the time integration. The von Neumann stability analysis of this numerical scheme is outlined in Appendix A.

Suppose the spatial domain is divided into  $n$  grid cells with the spatial grid size  $\Delta x$ . Arrays of nodal values for flow depth and  $Hu$ , respectively, are defined as

$$\mathbf{H} = (H_1, H_2, \dots, H_n)^T,$$

$$\mathbf{M} = (H_1 u_1, H_2 u_2, \dots, H_n u_n)^T.$$

With time increment  $\Delta t$  the fourth order Runge-Kutta scheme can be written as follows,

$$\mathbf{M}^1 = \mathbf{M}, \quad \mathbf{M}^2 = \mathbf{M} + \frac{\Delta t}{2} \mathbf{S}^1, \quad \mathbf{M}^3 = \mathbf{M} + \frac{\Delta t}{2} \mathbf{S}^2, \quad \mathbf{M}^4 = \mathbf{M} + \Delta t \mathbf{S}^3, \quad (8)$$

where  $\mathbf{M}^k$  are intermediate value arrays and  $\mathbf{S}^k$  are correspondingly arrays for the time derivatives of  $Hu$ , obtained by solving

$$(I - \bar{D})\mathbf{S}^k = -\bar{\Psi}(\mathbf{H}, \mathbf{M}^k), \quad \text{for } k = 1, \dots, 4. \quad (9)$$

Here  $\bar{\Psi}$  and  $\bar{D}$  represent centered spatial discretizations for the term  $\Psi$  and the operator  $D$ , respectively. These are given explitley below. Finally the value of  $\mathbf{M}$  at the new time level is obtained by

$$\mathbf{M}^+ = \mathbf{M} + \frac{\Delta t}{6} [\mathbf{S}^1 + 2\mathbf{S}^2 + 2\mathbf{S}^3 + \mathbf{S}^4]. \quad (10)$$

In (9),  $\bar{D}$  is a tri-diagonal  $n \times n$  matrix with elements

$$\bar{D}_{i,i-1} = \frac{1}{\Delta x^2} \left[ \left( B + \frac{1}{2} \right) h_i^2 - \frac{1}{6} \frac{h_i^3}{h_{i-1}} \right],$$

$$\bar{D}_{i,i} = \frac{1}{\Delta x^2} \left( -2B - \frac{2}{3} \right) h_i^2,$$

$$\bar{D}_{i,i+1} = \frac{1}{\Delta x^2} \left[ \left( B + \frac{1}{2} \right) h_i^2 - \frac{1}{6} \frac{h_i^3}{h_{i+1}} \right].$$

Correspondingly, the  $i$ -th element of  $\Psi(\bar{\mathbf{H}}, \mathbf{q})$  is

$$\begin{aligned}\bar{\Psi}_i = & \left( B + \frac{1}{2} \right) \frac{h_i^2}{2\Delta x^3} \left[ \left( \frac{M_{i+2}^2}{H_{i+2}} - 2\frac{M_{i+1}^2}{H_{i+1}} + 2\frac{M_{i-1}^2}{H_{i-1}} - \frac{M_{i-2}^2}{H_{i-2}} \right) \right. \\ & \left. + g(H_{i+1}(\eta_{i+2} - \eta_i) - 2H_i(\eta_{i+1} - \eta_{i-1}) + H_{i-1}(\eta_i - \eta_{i-2})) \right] \\ & - \frac{1}{6} \frac{h_i^3}{2\Delta x^3} \left[ \frac{M_{i+2}^2/H_{i+2} - M_i^2/H_i}{H_{i+1}} - 2\frac{M_{i+1}^2/H_{i+1} - M_{i-1}^2/H_{i-1}}{h_i} \right. \\ & \left. + \frac{M_i^2/H_i - M_{i-2}^2/H_{i-2}}{H_{i-1}} \right. \\ & \left. + g \left( \frac{H_{i+1}(\eta_{i+2} - \eta_i)}{H_{i+1}} - 2\frac{H_i(\eta_{i+1} - \eta_{i-1})}{h_i} + \frac{H_{i-1}(\eta_i - \eta_{i-2})}{H_{i-1}} \right) \right] \\ & - \frac{Bgh_i^2}{2\Delta x^3} (H_{i+1}(\eta_{i+2} - \eta_i) - 2H_i(\eta_{i+1} - \eta_{i-1}) + H_{i-1}(\eta_i - \eta_{i-2})),\end{aligned}$$

for  $i = 1, 2, \dots, n$ .

## 2.2. Models for comparison

The performance of the Boussinesq model presented here is assessed by comparison with numerical results from a full potential flow model which is described in Løvholt et al. (2013) and references therein. The model is based on a boundary integral technique and is run with fully nonlinear solitary wave solutions as initial conditions. During shoaling and breaking this model can describe the evolution of a plunger, but breaks down when the plunger reaches the free surface. Hence, the potential flow results are used to determine the point of breaking due to shoaling and to evaluate the evolution of amplitude and wave shape of the current model until this point. Below we refer to the full potential model as the BIM (Boundary Integral Method) model.

Comparison with a pre-existing, fully nonlinear Boussinesq model is facilitated by the application of a Lagrangian model, described in Løvholt et al. (2013). Apart from the use of Lagrangian coordinates the equations employed in this model are similar to (1) and (2). They differ only concerning the nonlinearities in the dispersion terms and that the dispersion optimization terms are added in a fully nonlinear fashion. Presently, the Lagrangian model has



145 no established bore capturing facility and is hence valid only to the point of  
 breaking. Results from this model will be referred to as 'Serre', even though  
 the dispersion enhancement is invoked.

Results for the Peregrine-type Boussinesq equations are obtained by the  
 GloBouss model. This is a dispersive tsunami propagation model which is based  
 150 on Peregrine-type equations and discretization on a staggered grid. Further  
 details are found in Løvholt et al. (2008).

For comparison also the version 2.1 of the FUNWAVE-TVD model by Shi  
 et al. (2012) is used. The FUNWAVE-TVD model shares important features  
 with BOUSSCLAW, employing a hybrid of the finite volume and finite difference  
 155 scheme to solve the fully non-linear higher order dispersive Boussinesq model  
 numerically. While we refer to Shi et al. (2012) for details, we briefly note  
 that FUNWAVE-TVD is based the fully nonlinear Boussinesq equations of Chen  
 (2006). The numerical spatial representation in FUNWAVE-TVD is MUSCL  
 TVD scheme to discretize for the flux and first order terms, whereas a cen-  
 160 tral finite difference scheme Wei et al. (1995) is utilized for the higher order  
 momentum terms. A Runge-Kutta scheme is employed for the time stepping.

### 3. Numerical Tests

#### 3.1. Solitary wave propagation

In order to validate the numerical approach a solitary wave propagation  
 is tested on a constant water depth. For the initial conditions, the analytic  
 solitary wave solution of the Serre's equations is used since analytic solutions  
 are unknown for the set (1) and (2). Solitary wave solutions to Serre's equations  
 are given as

$$\begin{aligned}\eta(x, t) &= A \operatorname{sech}^2(\kappa(x - ct)), \\ u(x, t) &= c \frac{\eta(x, t)}{h},\end{aligned}\tag{11}$$

where

$$\kappa = \frac{\sqrt{3h}}{2A\sqrt{A+h}}, \quad \text{and} \quad c = \sqrt{g(A+h)}.\tag{12}$$

In this expression,  $A$  and  $h$  are constants which represent the wave amplitude  
 165 and the undisturbed water depth respectively.

In Figure 1, snapshots from the BOUSSCLAW's simulation are shown at  $t =$   
 0, 4, 8 and 12 with  $\Delta x = 0.1$ . For the initial conditions, the solution (11) is  
 used with  $A = 0.2$ ,  $h = 1$  and  $g = 9.81$ . The computational results are in good  
 agreement with the analytic solutions concerning height, shape and propagation  
 170 speed. The amplitudes decreases very gently as the wave propagates.

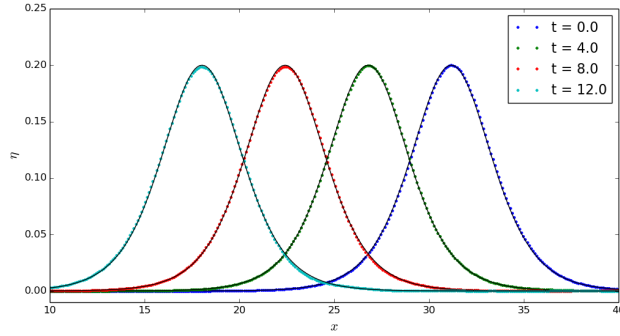


Figure 1: Snapshot of the analytic and computed solitary wave at  $t = 0, 4, 8$  and  $12$  with  $A/h = 0.2$ . The wave propagates from right to left, and the analytic solutions are black solid lines.

The wave energies for the shallow water equations and the Boussinesq equations are  $E_0$  and  $E_0 + E_1$ , respectively, where

$$E_0 = \frac{1}{2} (g\eta^2 + H\bar{u}^2), \quad (13)$$

$$E_1 = \frac{1}{6} H^3 \bar{u}_x^2 + \frac{1}{2} H^2 h_x \bar{u} \bar{u}_x + \frac{1}{2} H h_x^2 \bar{u}^2. \quad (14)$$

Details are given in (Madsen et al., 1997) and Appendix B.

In Figure 2a, the energy of the solitary wave is shown with  $A/h = 0.2$  and  $\Delta x = 0.2$ . There are fluctuations both in the potential and kinetic energy that is evident when we zoom in, and the total energy decreases showing that the numerical procedure has dissipation. In Figure 2b, the relative error of the

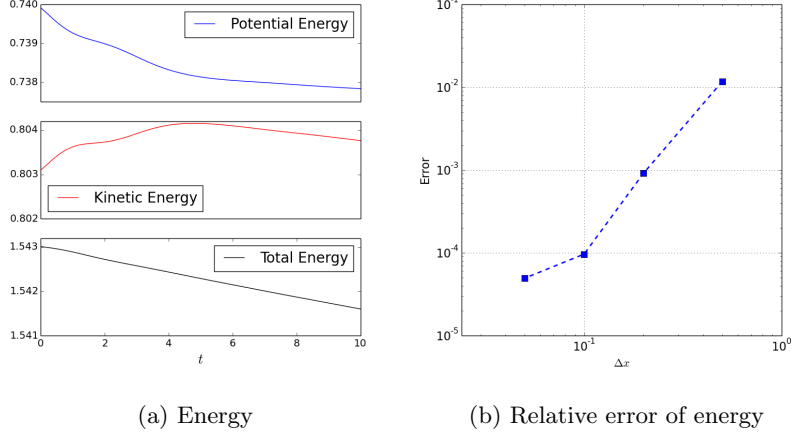


Figure 2: The energy of a solitary wave with  $\Delta x = 0.2$  (left), and log-log plot of relative error at  $t = 10$  for  $\Delta x = 0.05, 0.1, 0.2$  and  $0.5$  (right).

energy at  $t = 10$ ,

$$Error = \frac{|E_{t=0} - E_{t=10}|}{|E_{t=0}|},$$

is shown for different  $\Delta x$ . For a solitary wave on a constant depth, the energy dissipation decreases with the grid increments.

### 3.2. Waves on a composite slope

175 A physical model was constructed at the Coastal Hydraulic Laboratory of the U.S. Army Corps of Engineers in order to address beach erosion and severe flooding problems Briggs et al. (1995). The model beach consists of three piece-wise linear slopes of 1:53, 1:150, and 1:13 with a vertical wall at the shoreline as shown in Figure 3. In the laboratory, the wavemaker was located at 23.23  
180 m. The gauge data from three cases are provided where the ratio  $A/h$  is equal to 0.038, 0.259 and 0.681 with  $h = 21.8$  cm.

The second case with  $A/h = 0.259$  has been compared with the numerical tests which employed 400 grid points. To specify the incoming wave from the left boundary, the data at Gauge 4 were used for the wave height, and the  
185 corresponding velocity (11) was applied.

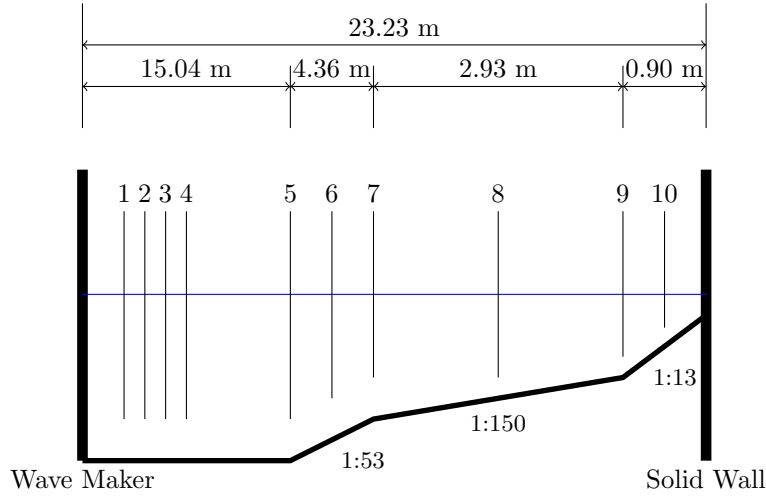


Figure 3: A sketch of the water tank

In Figure 4, water surface elevations at gauges 5, 7 and 8 are shown. The simulated waves are in good agreement with the laboratory measurements. For the reflected waves, larger discrepancies are observed. The increased discrepancy occurs because the full interaction between the wave and the wall at the right boundary is less accurately captured. Friction forces influence the wave evolution along the shallow region near the right wall, but we have not included these in the present numerical simulation. A better fit may possibly be obtained by incorporating friction, however, tuning the friction models is not the scope of this work.

#### 4. Simulation of wave steepening and breaking using a BIM model

Synolakis (1987) performed a series of laboratory experiments for the run-up of solitary waves on uniform slopes. Here, we are interested in the breaking cases. One such example in Synolakis (1987) is a solitary wave of amplitude  $A/h = 0.28$  approaching a slope of 1 : 19.85. In Figure 5, the initial set-up for a test is shown.

The set-up of the wave tank in the simulations follows the laboratory experiments by Synolakis (1987). The bathymetry of the wave tank is composed of a

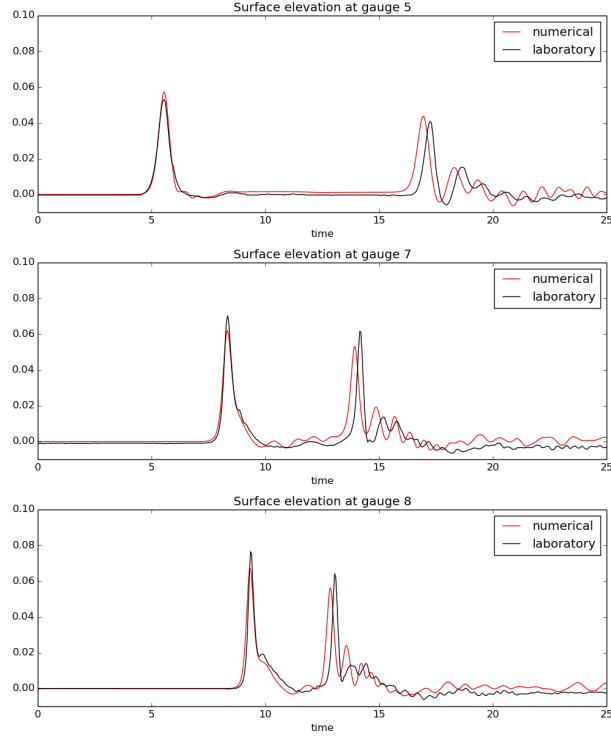


Figure 4: Water surface elevation at gauges 5,7 and 8 for  $A/h = 0.269$  case.

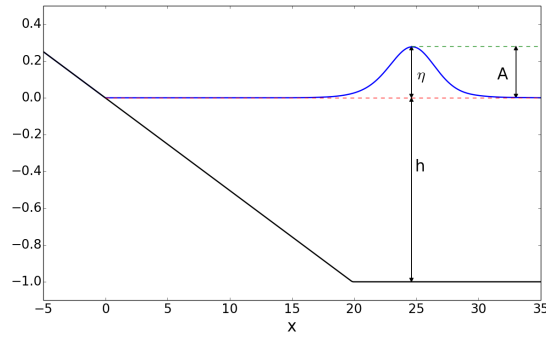


Figure 5: Set-up of a numerical test for Synolakis' experiments.

horizontal bottom and a uniform slope as shown in Figure 5. A solitary wave of  
amplitude  $A/h = 0.28$  is generated at the right end of the tank and propagates  
leftwards to the beach.

We present the results using the non-dimensional time  $t^* = t\sqrt{h/g}$  and non-dimensional space  $x^* = x/h$ . In the following, we drop the asterisks in the presentation of the results. In Synolakis (1987),  $t = 0$  was defined as when the wave crest was a non-dimensional distance,  $L$ , from the toe of the slope, where

$$L = \sqrt{\frac{4A}{3h}} \operatorname{arccosh} \left( \frac{1}{0.05} \right).$$

However, at  $t = 0$ , the solitary wave has an elevation of 5% of its maximum at the toe of the beach, meaning that the slope has started to interact with the solitary wave. To avoid any such interaction obscuring our analysis, we instead place the initial solitary wave using equation (11) at  $L + 5c$ , where  $c$  is the shallow water wave celerity. In this way, the initial solitary wave has a negligible interaction with the slope when initialized.

In Figure 6, the laboratory measurements are shown with the computational results from the BIM model for a breaking wave case of Synolakis with  $A/h = 0.28$  and 1 : 19.85 slope at  $t = 15$ .

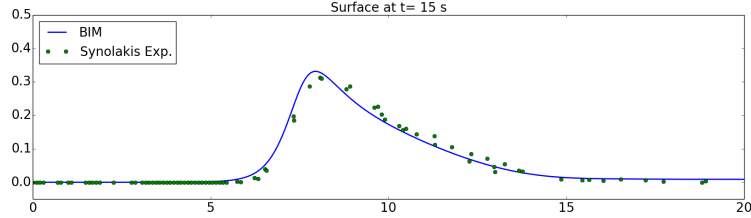


Figure 6: Comparison of the laboratory experiments and BIM at  $t=15$  with  $A/h = 0.28$  on a slope of 1 : 19.85.

Figure 7 shows the numerical results from the BIM model at  $t = 17, 18$  and 18.6. In the BIM results a vertical front is observed at  $x = 4.02$  and  $t = 18.6$  with the maximum wave amplitude  $A = 0.414$ , and this shows similarity with the analysis of Titov and Synolakis (1995) on the wave breaking point. The ratio of amplitude to depth,  $A/h$ , is about 2.01 at the break point. The potential flow model cannot be run much beyond the breaking points (until the attachment of the plunger only) and gives no information on the following bore propagation. In Figure 8, computations of the shallow water equations (present model without

the second fractional step) display a premature bore formation which checks the amplification during the subsequent shoaling. As a consequence the amplitude in the shallow water equations simulation is markedly smaller than that of the potential flow model when the latter indicates breaking.

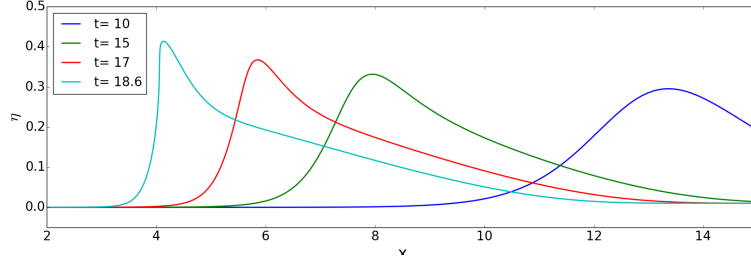


Figure 7: Computational results from BIM of a wave with  $A/h = 0.28$  on a slope of 1 : 19.85. A vertical front is observed at  $t = 18.6$ .

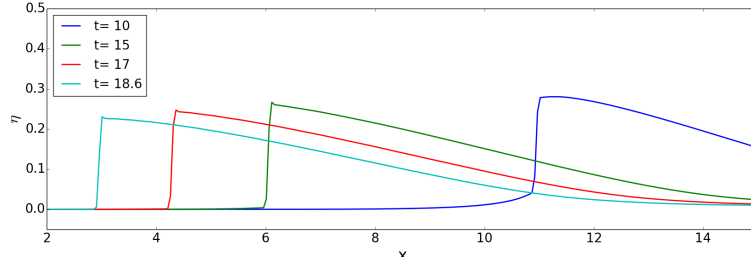


Figure 8: Computational results from NLSW at  $t = 10, 15, 17$  and  $18.6$ .

## 5. Pre-breaking and breaking wave evolution using depth averaged models

We use the set-up described in section 4 for the Boussinesq modeling of solitary waves on a slope. Figure 9 shows the snapshots of the water surface at  $t=16$  and  $18.6$  from BIM and BOUSSCLAW with  $B=0$  and  $1/15$ . When the wave is smooth at  $t=16$ , the BOUSSCLAW results are similar. At the breaking point,  $t = 18.6$ , larger differences are observed. If  $B = 0$ , the wave speed is slightly faster than the BIM result, but the wave amplitude is similar. When

235  $B = 1/15$ , the wave speed matches the BIM results better, but the amplitude is slightly smaller. In general, the computational results are rather similar with  $B = 0$  and  $1/15$ .

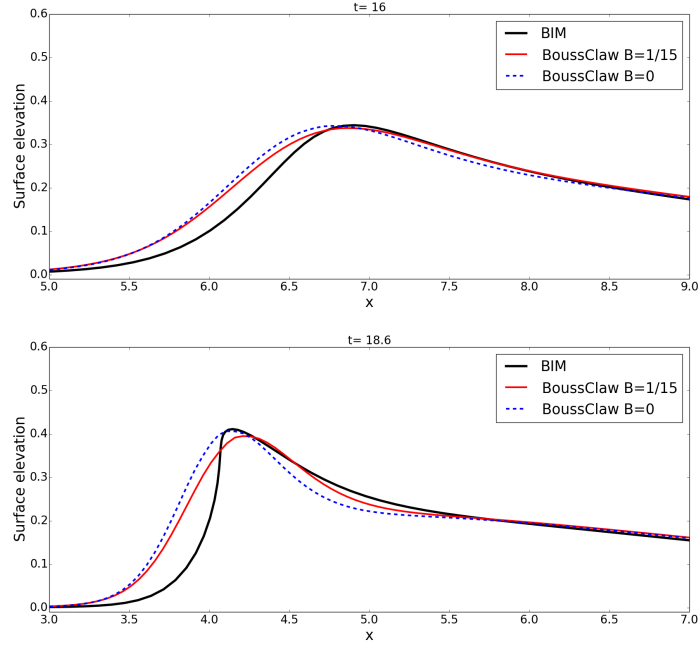


Figure 9: Snapshots of BIM and BOUSSCLAW with  $B=0$  and  $1/15$  at  $t=16$ , and  $18.6$ .

Next, the BOUSSCLAW simulations are compared with those of other Boussinesq solvers, namely FUNWAVE (Shi et al., 2012), GLOBOUSS (Løvholt et al., 2010) and the Serre type formulation (Løvholt et al., 2013). As noted above, the original Serre's equations are enhanced by adding the Schäffer et al. (1993) terms.

In Figure 10, snapshots from different numerical models are shown at  $t=15$ , 17 and 18. At  $t=15$ , the computational results from different numerical tools show slightly different results, but the general pattern is similar. At  $t=17$ , some discrepancies are observed that can be split into two groups, and GLOBOUSS and FUNWAVE are similar while BOUSSCLAW and Serre's results are similar. The wave amplitudes computed by GLOBOUSS and FUNWAVE, are more than 10 %



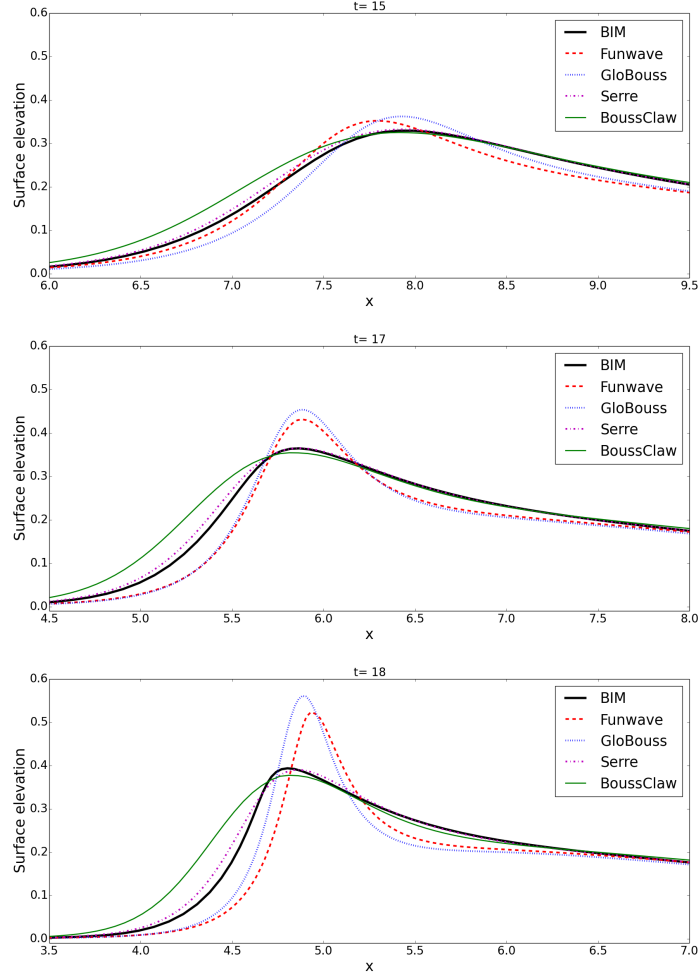


Figure 10: Snapshots of BIM, Serre, GLOBOUSS, BOUSSCLAW and FUNWAVE at  $t = 15$ , 17 and 18. The BOUSSCLAW is used with  $B=1/15$ , and the Peregrine's form is used for GLOBOUSS.

larger than BIM. The wave amplitude continues to increase with GLOBOUSS and FUNWAVE simulations, and the difference from the BIM result becomes larger at  $t = 18$ . The results from the Serre and BOUSSCLAW models clearly more similar to those of the BIM model. Especially, the wave amplitudes are correctly determined by these models.

### 5.1. Wave Breaking

255 In order to catch wave breaking in a heuristic fashion, we may choose to  
 invoke the threshold  $\epsilon_B := \eta/h$  for BOUSSCLAW. When the threshold is reached,  
 the wave breaking is supposed to be initiated, and the dispersive terms are  
 suppressed. At the breaking, the set of equations is locally switched to the  
 shallow water equations for the corresponding wave packet, and the trailing  
 260 waves are solved with the Boussinesq equations if the thresholds are not reached.  
 In the numerical simulation of the BOUSSCLAW model, the ratio  $\epsilon_B$  reaches the  
 threshold 0.8 at  $t = 14.9$  when the peak of the wave is at  $x = 8.03227$ . In the  
 following, we explore the wave evolution with and without the application of  
 this threshold.

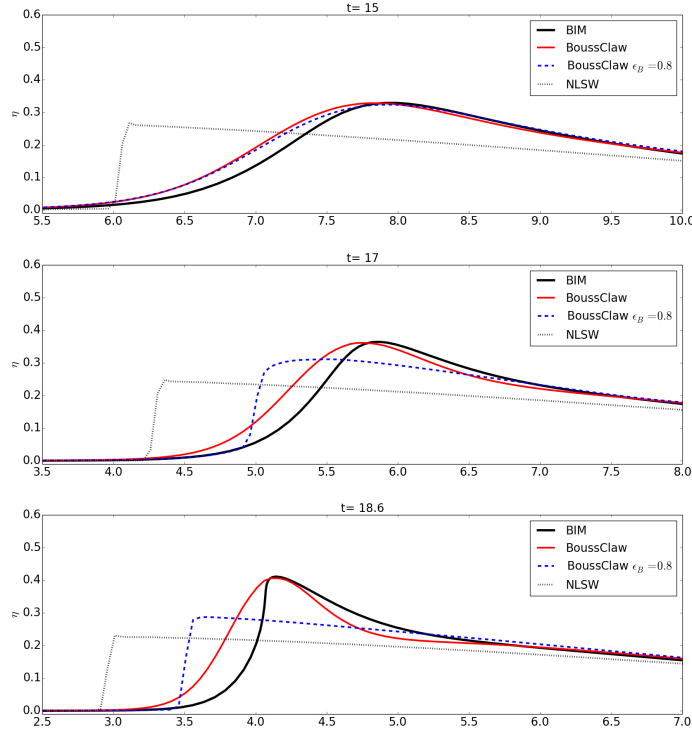


Figure 11: Comparison of BIM, BOUSSCLAW and NLSW with  $\epsilon_B = 0.8$  at  $t=15, 17$  and  $18.6$ .

265 In Figure 11, snapshots are shown at  $t=15, 17$ , and  $18.6$  from BIM, BOUSS-

CLAW and NLSW. At  $t=15$ , the difference between BIM and BOUSSCLAW is small, but the difference becomes noticeable in the wave shape and amplitude at  $t = 17$  and  $18.6$ . As the governing equations are switched to the shallow water equations, the a bore is forming, and the wave amplitude decreases.

270 Figure 12 shows the amplitude to depth ratio,  $\epsilon_B$ , as function of the crest location. With BIM simulations, the wave starts breaking at  $x = 4.09$ . When the crest in the BOUSSCLAW simulation reaches  $x = 4.09$  we find  $A/h = 1.97$ , the ratio of wave speed to celerity ( $u/\sqrt{gH}$ ) is 1.034 and maximum surface slope angle of  $39.1^\circ$ .

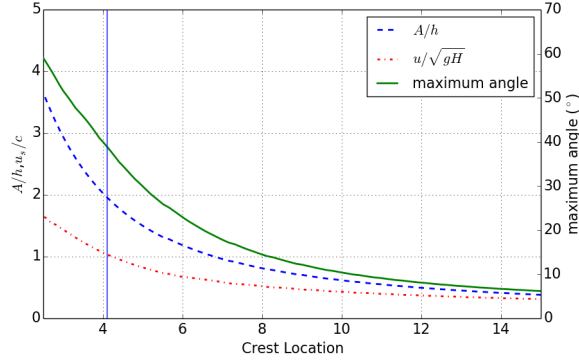


Figure 12: Plot of  $A/\eta$ ,  $u_s/c$  and maximum angle of waves vs. crest location. BIM shows the wave break at  $x = 4.09$ .

## 275 5.2. Wave Run-up

When a wave reaches a coastline, the coastline changes in time as the wave runs up the slope and recedes eventually. For the numerical simulations, it has been a challenge to compute the inundation correctly. In the BOUSSCLAW, the governing equations are locally switched to the shallow water equation solver  
 280 GEOCLAW near the coastline. The GEOCLAW software can handle the wet and dry states, and it has the depth positivity property via the HLLE solver. Details can be found at George (2008).

If friction terms are not included, the run-up heights of the numerical tests are higher than the experiments. For example, the bottom left panel of Figure

13 shows that the run-up height without the friction terms is much larger than the experiments. We use the Manning friction as follows,

$$f_D = -\frac{gC_d^2 u|u|}{H^{5/3}},$$

where  $C_d$  is a Manning drag coefficient. For the numerical simulations, a threshold for the dry state needs to be chosen. If the water depth is smaller than this threshold,  $H < d^*$ , then we set  $H = 0$ . In this paper, we use  $C_d = 0.02$ , and the dry tolerance depth is set as  $d^* = 10^{-4}$ .

Antuono et al. (2012) derived an approximate solution of the shoreline for the shallow water equations with the Chezy friction, and showed the effect of the frictional coefficient and the water depth tolerance.

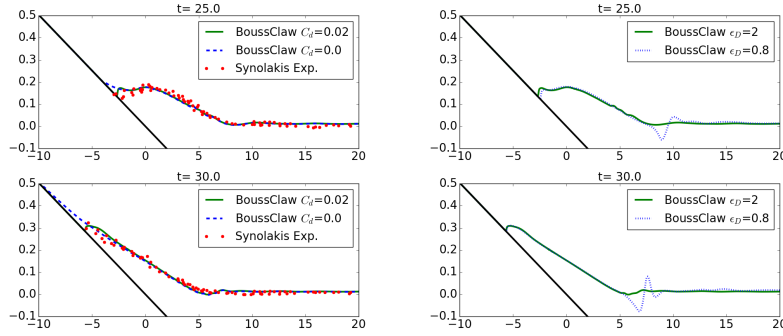


Figure 13: BoussClaw results at  $t=25$  and  $30$ . On the left column,  $\epsilon_D$  is fixed at  $2$ , and on the right column,  $C_d$  is fixed at  $0.02$ .

Figure 13 shows the effect of the parameters  $C_d$  and  $\epsilon_D$ . On the left column, snapshots at  $t=25$  and  $30$  are shown with  $C_d = 0$  and  $0.02$ , and the experiment of Synolakis (1987) is shown as red dots. The numerical result is in a good agreement with the experiment when  $C_d = 0.02$ . On the right column, the BOUSSCLAW results are shown with  $\epsilon_D = 0.8$  and  $2$ . The run-up heights with different  $\epsilon_D$  are comparable, but small dispersive waves are observed for  $\epsilon_D = 0.8$ .

### 5.3. Wave Energy

The wave energy is nearly conserved when the wave is smooth, but decreases as the wave breaks. The wave energy expressions for the shallow water equations and Boussinesq equations are  $E_0$  and  $E_0 + E_1$  respectively, which are given in (13) and (14).

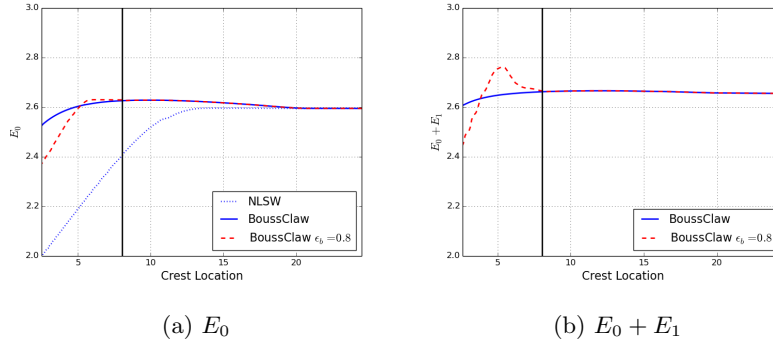


Figure 14: Energy plots of NLSW and BOUSSCLAW. The vertical line is at  $x = 8.03227$  m where  $\epsilon_B = 0.8$ , and the governing equations are switched to the NLSW from the Boussinesq equations.

In Figure 14, the wave energy  $E_0$  and  $E_0 + E_1$  are shown. The energy denotes the aggregate of the wave energy in the entire computational domain and is shown as function of the crest location. In the left panel, the energy  $E_0$  is well-preserved for the shallow water equations before the wave forms a shock, and then the energy dissipates after a shock is formed. In the right panel,  $E_0 + E_1$  is well-preserved for the BOUSSCLAW simulation during deep water propagation, but the value decreases slightly as the wave steepens near the shoreline. When the threshold  $\epsilon_B = 0.8$  is used, the energy  $E_0 + E_1$  is well-preserved as shown on the right figure before the threshold is reached. When the crest is located at  $x = 8.03227$  with  $\epsilon_B = 0.8$ , the wave energy  $E_0$  on the left figure does not decrease immediately. The energy  $E_0$  is preserved for a while, then starts to decrease as a shock is formed.

## 6. Conclusion

315 In the present paper we have presented a new operational Boussinesq type  
model, BOUSSCLAW, for modeling fully non-linear dispersive tsunami propaga-  
tion, taking also into account drying-wetting during inundation and withdrawal  
on the beach. BOUSSCLAW resembles much used operational models such as  
FUNWAVE-TVD and COULWAVE-TVD, but is based on a slightly simpler and  
320 more transparent set of governing equations, and has a slightly different nu-  
merical scheme. We have tested numerical implementation towards analytical  
solitary wave expressions as well as laboratory experiments.

Making use of the experiments of Synolakis (1987) enabled us to constrain  
a set of different long wave models, including BOUSSCLAW, as well as a full  
325 potential BIM reference model. Using the BIM, we were able to explore in detail  
the post-breaking behaviour, and to identify the point of breaking accurately.  
This was useful for determining the validity of the respective long wave models.  
First, we found that by using standard NLSW models, the point of breaking  
will be located too far offshore. Boussinesq models provide the opportunity  
330 of providing a more accurate description of the near shore propagation and  
shoaling. However, in current practise the Boussinesq terms are often omitted  
near shore through the  $A/h > 0.8$  threshold criteria. As a consequence, the  
point of breaking may be misinterpreted also in Boussinesq type models.

In the present example, we investigated the near shore propagation over  
335 a relatively gentle shelf of  $1/19.85$  slope, and in this case the actual onset of  
breaking occurred for  $A/h \approx 2$ , which is significantly later than what would be  
predicted in any standard approach (NLSW or Boussinesq). As demonstrated  
in this paper, the combined effects of non-linearities and dispersion influence the  
solution markedly, when accumulated to the point of breaking. It is noted that  
340 the artificial effect discovered would depend on the slope, and the  $A/h = 0.8$   
limited may well work better on a much gentler slope as it is primarily derived  
based on solitary wave evolution on constant depth. On the other hand,  $1/19.85$   
slope is already quite gentle, and the offset between the reference solution and

Boussinesq models using this criteria may be even more pronounced for steeper  
345 slopes.

## References

- V. V. Titov, C. E. Synolakis, Modeling of breaking and nonbreaking long-wave evolution and runup using VTCS-2, *Journal of Waterway, Port, Coastal, and Ocean Engineering* 121 (6) (1995) 308–316.
- 350 F. Imamura, Long-wave runup models, chapter Simulation of wave-packet propagation along sloping beach by TUNAMI-code, *World Scientific* 3 (1996) 4.
- S. Harig, Chaeroni, W. S. Pranowo, J. Behrens, Tsunami simulations on several scales, *Ocean Dynamics* 58 (5) (2008) 429–440, ISSN 1616-7228.
- M. J. Berger, D. L. George, R. J. LeVeque, K. T. Mandli, The GeoClaw software  
355 for depth-averaged flows with adaptive refinement, *Adv. Water Res.* 34 (2011) 1195–1206.
- J. Borrero, K. Sieh, M. Chlieh, C. E. Synolakis, Tsunami inundation modeling for western Sumatra, *Proceedings of the National Academy of Sciences of the United States of America* 103 (52) (2006) 1967319677.
- 360 G. Kaiser, L. Scheele, A. Kortenhaus, F. Løvholt, H. Römer, S. Leschka, The influence of land cover roughness on the results of high resolution tsunami inundation modeling, *Natural Hazards and Earth System Sciences* 11 (2011) 2521–2540.
- A. Hooper, J. Pietrzak, W. Simons, J. Cui, R. Riva, M. Naeije, T. A., van  
365 Scheltinga, E. Schrama, G. Stelling, S. A., Importance of horizontal seafloor motion on tsunami height for the 2011 Mw=9.0 Tohoku-Oki earthquake, *Earth and Planetary Science Letters* 361 (1) (2013) 469–479.
- F. Romano, E. Trasatti, S. Lorito, C. Piromallo, A. Piatanesi, Y. Ito, D. Zhao, K. Hirata, P. Lanucara, , M. Cocco, Structural control on the Tohoku earth-

- 370     quake rupture process investigated by 3D FEM, tsunami and geodetic data,  
Sci. Rep. 4 (5631).
- S. Glimsdal, G. Pedersen, C. Harbitz, F. Løvholt, Dispersion of tsunamis: does  
it really matter?, Nat. Hazards Earth Syst. Sci. 13 (2013) 1507–1526.
- F. Løvholt, G. Pedersen, C. Harbitz, S. Glimsdal, J. Kim, On the characteristics  
375     of landslide tsunamis, Phil. Trans. R. Soc. A 373 (2053) (2015) 20140376.
- J. Behrens, F. Dias, New computational methods in tsunami science, Phil.  
Trans. R. Soc. A 373 (2053) (2015) 20140382.
- P. A. Madsen, O. R. Sørensen, A new form of the Boussinesq equations with im-  
proved linear dispersion characteristics. Part 2. A slowly-varying bathymetry,  
380     Coastal Engineering 18 (3) (1992) 183–204.
- O. Nwogu, Alternative form of Boussinesq equations for nearshore wave prop-  
agation, Journal of waterway, port, coastal, and ocean engineering 119 (6)  
(1993) 618–638.
- D. H. Peregrine, Long waves on a beach, Journal of Fluid Mechanics 27 (04)  
385     (1967) 815–827.
- A. B. Kennedy, Q. Chen, J. T. Kirby, R. A. Dalrymple, Boussinesq modeling  
of wave transformation, breaking, and run-up. Part I: 1D., J. Waterw., Port,  
Coast., Ocean Engrg. 126 (1) (2000) 39–47.
- F. Løvholt, P. Lynett, G. K. Pedersen, Simulating run-up on steep slopes with  
390     operational Boussinesq models; capabilities, spurious effects and instabilities,  
Nonlin. Processes Geophys. 20 (2013) 379–395.
- H. A. Schäffer, P. A. Madsen, R. Deigaard, A Boussinesq model for waves  
breaking in shallow water, Coastal Engineering 20 (3) (1993) 185–202.
- P. J. Lynett, Nearshore wave modeling with high-order Boussinesq-type equa-  
395     tions, Journal of Waterway, Port, Coastal, and Ocean Engineering 132 (5)  
(2006) 348–357.



- M. Tissier, P. Bonneton, F. Marche, F. Chazel, D. Lannes, A new approach to handle wave breaking in fully non-linear Boussinesq models, *Coastal Engineering* 67 (2012) 54–66.
- 400 M. Matsuyama, M. Ikeno, T. Sakakiyama, T. Takeda, A study of tsunami wave fission in an undistorted experiment, *Pure and Applied Geophysics* 164 (2-3) (2007) 617–631.
- K. Erduran, S. Ilic, V. Kutija, Hybrid finite-volume finite-difference scheme for the solution of Boussinesq equations, *Int. J. for Num. Meth. in Fluids* 49  
405 (2005) 1213–1232.
- D.-H. Kim, P. Lynett, S. Socolofsky, A depth-integrated model for weakly dispersive, turbulent, and rotational flows, *Ocean Modelling* 27 (2009) 198–214.
- F. Shi, J. T. Kirby, J. C. Harris, J. D. Geiman, S. T. Grilli, A high-order adaptive time-stepping TVD solver for Boussinesq modeling of breaking waves and  
410 coastal inundation, *Ocean Modelling* 43 (2012) 36–51.
- M. Tonelli, M. Petti, Hybrid finite volume–finite difference scheme for 2DH improved Boussinesq equations, *Coastal Engineering* 56 (5) (2009) 609–620.
- P. J. Lynett, T. R. Wu, P. L. F. Liu, Modeling wave runup with depth-integrated equations, *Coastal Engineering* 46 (2) (2002) 89–107.
- 415 G. Wei, J. T. Kirby, Time-dependent numerical code for extended Boussinesq equations, *Journal of Waterway, Port, Coastal, and Ocean Engineering* 121 (5) (1995) 251–261.
- Clawpack Development Team, Clawpack software, URL <http://www.clawpack.org>, version 5.3.1, 2016.
- 420 R. J. LeVeque, Wave propagation algorithms for multidimensional hyperbolic systems, *Journal of Computational Physics* 131 (2) (1997) 327–353.

- D. L. George, Augmented Riemann solvers for the shallow water equations over variable topography with steady states and inundation, *Journal of Computational Physics* 227 (6) (2008) 3089–3113.
- 425 M. Tissier, P. Bonneton, F. Marche, F. Chazel, D. Lannes, Serre Green-Naghdi modelling of wave transformation breaking and run-up using a high-order finite-volume finite-difference scheme, *Coastal Engineering Proceedings* 1 (32) (2011) 13.
- 430 D. Dutykh, T. Katsaounis, D. Mitsotakis, Finite volume methods for unidirectional dispersive wave models, *International Journal for Numerical Methods in Fluids* 71 (6) (2013) 717–736.
- R. J. LeVeque, *Finite volume methods for hyperbolic problems*, vol. 31, Cambridge university press, 2002.
- 435 F. Løvholt, G. Pedersen, G. Gisler, Oceanic propagation of a potential tsunami from the La Palma Island, *J. Geophys. Res.* 113 (2008) C09026.
- Q. Chen, Fully nonlinear Boussinesq-type equations for waves and currents over porous beds, *J. of Eng. Mech., ASCE* 132 (2) (2006) 220–230.
- 440 G. Wei, J. T. Kirby, S. T. Grilli, R. Subramanya, A fully nonlinear Boussinesq model for surface waves. Part 1. Highly nonlinear unsteady waves, *J. Fluid Mech.* 294 (1995) 71–92.
- P. A. Madsen, O. Sørensen, H. Schäffer, Surf zone dynamics simulated by a Boussinesq type model. Part I. Model description and cross-shore motion of regular waves, *Coastal Engineering* 32 (4) (1997) 255–287.
- 445 M. Briggs, C. Synolakis, U. Kanoglu, D. Green, Runup of solitary waves on a vertical wall, *Costal Hydraulics Laboratory*, URL <http://chl.erd.c.usace.army.mil/chl.aspx?p=s&a=Projects;36>, 1995.
- C. E. Synolakis, The runup of solitary waves, *Journal of Fluid Mechanics* 185 (1987) 523–545.

F. Løvholt, G. Pedersen, S. Glimsdal, Coupling of Dispersive Tsunami Prop-  
 450 agation and Shallow Water Coastal, Open Oceanography Journal 4 (2010)  
 71–82.

M. Antuono, L. Soldini, M. Brocchini, On the role of the Chezy frictional term  
 near the shoreline, Theoretical and Computational Fluid Dynamics 26 (1-4)  
 (2012) 105–116.

455 T. B. Benjamin, J. L. Bona, J. J. Mahony, Model equations for long waves in  
 nonlinear dispersive systems, Philosophical Transactions of the Royal Society  
 of London A: Mathematical, Physical and Engineering Sciences 272 (1220)  
 (1972) 47–78.

## Appendix A. Stability of the hybrid scheme

It is difficult to analyze the numerical stability for our full Boussinesq equa-  
 tions. To obtain some insight in the stability of the proposed hybrid numerical  
 scheme, we thus consider a closely related, but simpler, equation, namely the  
 linearized Benjamin-Bona-Mahony (BBM) equation (Benjamin et al. (1972))

$$u_t + cu_x = \frac{h^2}{6}u_{txx}, \quad (\text{A.1})$$

460 where  $c = \sqrt{gh}$ . This equation describes weakly dispersive, uni-directional waves  
 in constant depth. The equation replaces the momentum equation, whereas no  
 separate continuity equation is involved.

Following the steps of section 2.1.2, we rearrange the equation (A.1) as

$$(I - D)(u_t + cu_x) + Du_x = 0, \quad (\text{A.2})$$

where  $D = \frac{h^2}{6}\partial_x^2$ . The first step of hybrid scheme for this equation is integration  
 of the advection equation

$$u_t + cu_x = 0, \quad (\text{A.3})$$

by the finite volume method. Then the Runge-Kutta method is applied to,

$$(1 - D)u_t + cDu_x = 0. \quad (\text{A.4})$$

which is the counterpart to (7).

If we use the centered spatial difference approximation of  $O(\Delta x^2)$  accuracy  
 465 on a regular grid we may employ a standard von Neumann analysis where we  
 calculate the growth of an harmonic mode over a single time step. Expressing  
 the coefficients of the velocity array before the time step as  $u_j = e^{i\xi j \Delta x}$  we then  
 replace the coefficient of  $\mathbf{M}^q$ , defined in section 2.1.2, by  $M_j^q = U_j^q = g^q e^{i\xi j \Delta x}$ ,  
 where  $q$  is 1, 2, 3, 4 or +. Correspondingly, the coefficients of the  $\mathbf{S}^k$  array,  
 470 which contains auxiliary, nodal values for  $u_t$ , is expressed  $(S_j^k) = s^k e^{i\xi j \Delta x}$ .

The stability of the first step, (A.3), is assured by the standard CFL criterion

$$\frac{c\Delta t}{\Delta x} < 1.$$

If we instead solve the NLSW equations, as in BoussClaw,  $c$  must be replaced by  
 the nonlinear characteristic velocity, which may lead to a more strict criterion.  
 However, the method employed in the first step is not suited for a von Neumann  
 stability analysis and we thus apply this technique to the second step only.  
 Hence, we may put  $g^1$  to unity, but it is preferable to retain it in the calculations.  
 The Runge-Kutta scheme for time stepping, (8), may now be expressed as

$$g^2 = g^1 + \frac{\Delta t}{2} s^1, \quad g^3 = g^1 + \frac{\Delta t}{2} s^2, \quad g^4 = g^1 + \Delta t s^3, \quad (\text{A.5})$$

The discrete version of (A.4), which is the counterpart to (9) for the BBM  
 equation reads

$$S_j^k - \frac{h^2}{6} \frac{S_{j+1}^k - 2S_j^k + S_{j-1}^k}{\Delta x^2} = -\frac{ch^2}{6} \frac{U_{j+2}^k - 2U_{j+1}^k + 2U_{j-1}^k - U_{j-2}^k}{2\Delta x^3},$$

which, inserted the harmonic expressions, implies

$$s^k = i \frac{\gamma}{\Delta t} g^k, \quad \gamma = c\Delta t \frac{2 \sin(\xi \Delta x)(1 - \cos(\xi \Delta x))}{6\Delta x^3 h^{-2} + 2\Delta x(1 - \cos(\xi \Delta x))}, \quad (\text{A.6})$$

where the  $\Delta t$  factors are included for convenience. The assembling of the inter-  
 mediate values in the Runge-Kutta procedure, (10), now yields

$$g^+ = g^1 + \frac{\Delta t}{6} [s^1 + 2s^2 + 2s^3 + s^4]. \quad (\text{A.7})$$

By combination of (A.5) and (A.6)  $s^k$  and  $g^k$ ,  $k = 1..4$  can be calculated successively and combined in (A.7) to provide the value of  $g^+$ ,

$$\begin{aligned} g^+(\gamma) &= \left(1 - \frac{1}{2}\gamma^2 + \frac{\gamma^4}{24} + \left(\frac{\gamma^3}{6} - \gamma\right)i\right) g^1 \\ |g^+(\gamma)|^2 &= \left(1 + \frac{1}{4}\gamma^4 + \frac{\gamma^8}{24^2} - \gamma^2 + \frac{\gamma^4}{12} - \frac{\gamma^6}{24} + \gamma^2 + \frac{\gamma^6}{36} - \frac{\gamma^4}{3}\right) |g^1|^2 \\ &= \left(1 - \frac{1}{72}\gamma^6 + \frac{1}{576}\gamma^8\right) |g^1|^2. \end{aligned}$$

Stability requires  $|g^+(\gamma)/g^1| < 1$  which is equivalent to  $|\gamma| < 2\sqrt{2}$ . Moreover, it is easily seen that  $\gamma < c\Delta t/\Delta x$ . Hence, a sufficient condition for stability of the second step of the hybrid scheme is

$$\frac{c\Delta t}{\Delta x} < 2\sqrt{2}.$$

This is more relaxed than the CFL condition for the advection equation (A.3). Therefore, if the CFL condition is satisfied in the advection equation, the fractional step is always stable with the suggested numerical scheme.

## Appendix B. Energy estimates and dissipation

### 475 Appendix B.1. Velocity field

To derive the energy estimates for the Boussinesq-type equations, we define the depth-averaged velocity as,

$$\bar{u} = \frac{1}{H} \int_{-h}^{\epsilon\eta} u dz.$$

Then the velocity  $u$  can be expressed as  $u = \bar{u} + \mu^2 u_1$  where

$$\int_{-h}^{\epsilon\eta} u_1 dz = 0. \quad (\text{B.1})$$

Then the kinematic boundary condition at the bottom and zero divergence implies

$$w = -h_x u - \bar{u}_x(z+h) + O(\mu^2).$$

## Appendix B.2. Energy integrals

The potential energy density per horizontal area is

$$V = \int_{-h}^{\epsilon\eta} gz dz = \frac{1}{2}\epsilon^2 g\eta^2 - \frac{1}{2}gh^2,$$

where the last term  $\frac{1}{2}gh^2$  is the equilibrium energy. The kinematic energy density has two contributions,

$$T = T_u + T_w; \quad T_u = \frac{1}{2}\epsilon^2 \int_{-h}^{\epsilon\eta} u^2 dz, \quad T_w = \frac{1}{2}\epsilon^2 \mu^2 \int_{-h}^{\epsilon\eta} w^2 dz.$$

For the horizontal part,  $T_u$  is

$$T_u = \frac{1}{2}\epsilon^2 \int_{-h}^{\epsilon\eta} u^2 dz = \frac{1}{2}\epsilon^2 \int_{-h}^{\epsilon\eta} \bar{u}^2 + 2\mu^2 \bar{u}u_2 + \mu^4 u_1^2 dz = \frac{1}{2}\epsilon^2 H \bar{u}^2 + O(\epsilon^2 \mu^4),$$

since  $\bar{u}$  is independent of  $z$  and by (B.1). Assuming  $\frac{1}{H} \int_{-h}^{\epsilon\eta} u^2 dz = \bar{u}^2$ , the vertical part is

$$\begin{aligned} T_u &= \frac{1}{2}\epsilon^2 \mu^2 \int_{-h}^{\epsilon\eta} h_x^2 u^2 + 2h_x u \bar{u}_x (z+h) + \bar{u}_x^2 (z+h)^2 dz + O(\epsilon^2 \mu^4) \\ &= \frac{1}{2}\epsilon^2 \mu^2 H \left( h_x^2 \bar{u}^2 + H h_x \bar{u} \bar{u}_x + \frac{1}{3} H^2 \bar{u}_x^2 \right) + O(\epsilon^2 \mu^4). \end{aligned}$$

Thus the energy of a wave can be approximated as

$$E = \epsilon^2 (E_0 + \mu^2 E_1 + O(\mu^4))$$

where

$$\begin{aligned} E_0 &= \frac{1}{2} (g\eta^2 + H \bar{u}^2), \\ E_1 &= \frac{1}{6} H^3 \bar{u}_x^2 + \frac{1}{2} H^2 h_x \bar{u} \bar{u}_x + \frac{1}{2} H h_x^2 \bar{u}^2. \end{aligned}$$